Design and multi-physics optimization of a novel MR damper with a variable resistance gap

Jiajia Zheng[1], Yancheng Li[2], and Jiong Wang[1]

[1] School of Mechanical Engineering, Nanjing University of Science and Technology, Nanjing, China
[2]School of Civil and Environmental Engineering, University of Technology, Sydney, Australia

Abstract

This paper presents the design and multi-physics optimization of a novel multi-coil magnetorheological (MR) damper with a variable resistance gap (VRG-MMD). Enabling the four electromagnetic coils (EMs) with individual exciting currents, a simplified magnetic equivalent circuit was presented and the magnetic flux generated by each voltage source passing through each active gap were calculated as vector operations. To design the optimal geometry of the VRG-MMD, the multi-physics optimization problem including electromagnetics and fluid dynamics has been formulated as a multi-objective function with weighting ratios among total damping force, dynamic range and inductive time constant. Based on the selected design variables (DVs), six cases with different weighting ratios have been optimized using Bound Optimization BY Quadratic Approximation (BOBYQA) technique. Finally, the vibration performance of the optimal VRG-MMD subjected to sinusoidal and triangle displacement excitations was evaluated compared with that of the typical multi-coil MR damper.

KEY WORDS

MR damper; variable resistance gap; multi-physics; optimization;

1. Introduction

Magnetorheological (MR) dampers with different operation principles have been widely utilized in various vibration control systems, such as vehicle suspension systems (Du et al.[1]; Hiemenz et al. [2]), seismic protection of cable-stayed bridges (Ok et al. [3]; Muhammad et al., 2005,[4]), aircraft landing gear systems (Batterbee et al. [5]; Batterbee et al. [6]; Powell et al.[7]) and advanced prosthetic systems (Gudmundsson et al. [8]; Xie et al. [9]). Similar to passive hydraulic dampers, the MR damper reduces the resistance of movements by pushing fluid through an orifice back and forth to deplete the kinetic energy (Mao et al. [10]; Bai et al. [11]). It is worth noting that smart magnetorheological fluids are employed and characterized as stable suspensions of 0.3-10 micron sized particles dispersed in non-magnetic carrying fluids, usually a synthetic hydrocarbon (Peng and Li [12]). In order to develop a magnetic field in the annular orifice, an electromagnet is usually incorporated into the piston and the reservoirs are filled with magnetorheological fluids (Du et al.[1]; Bai et

Email: znjust_cn@163.com

al. [11]). With the application of the exciting current through the wire leads, the apparent viscosity of the MR fluid is increased dramatically by forming a yield stress as the magnetic flux passes through it. Therefore, by controlling the input exciting current, the controllable force can be altered according to a command from the controller (Singh et al. [13]).

Much research has been focused on the modelling and testing of the MR dampers, however, few attention has been paid to the geometric optimization of these dampers. The optimization problem is expected to figure out the optimal configuration of the MR damper within a constraint on the volume of the cylinder by minimizing a proposed objective function. This is quite challenging because many factors such as the damping force, dynamic range, and the inductive time constant must be considered when forming the optimization problem. Typically, the objective functions have been defined as the valve ratio (Nguyen et al. [14]), control energy consumption and response time (Nguyen et al. [15]), total damping force (Yang et al. [16]), dynamic range (Parlak et al. [17]) and equivalent non-dimensional damping coefficient (Rosenfeld and Wereley, [18]).

Since the abovementioned objective function partially depends on the yield strength of the magnetorheological fluid, it is required to evaluate the magnetic field generated within the damper. So far, two approaches have been utilized: analytical calculation and finite element based computation. For example, Rosenfeld and Wereley (Rosenfeld and Wereley, [18]) optimized a volume-constrained MR valve by proposing an analytical design method which was relied on the assumption that constant magnetic flux passed through the magnetic circuit. However, for the MR damper with a complex geometry, one cannot obtain accurate results from simplified assumptions. On the other hand, by taking its advantages, the FE based method has been popularly employed to compute the magnetic circuit for the optimization problem (Nguyen et al. [14]; Nguyen et al. [15]; zhang et al. [19]). Nguyen et al. utilized ANSYS software to minimize the valve ratio, control energy (Nguyen et al. [14]; Nguyen et al. [15]) and a multi-objective function (Nguyen et al. [20]; Nguyen et al. [21]) for different types of the MR valves, including single-coil, two-coil, three-coil and radial/annular. By employing a multi-disciplinary design optimization (MDO) procedure based on finite element method, Karakoc et al. [22] analyzed the magnetic field and heat distribution of an automatic MR brake and obtained the optimal geometric parameters for maximum braking torque. Parlak et al. [23] proposed a new method which employs both electromagnetics and CFD to achieve the desired damper force and maximum controllability of the MR damper via finite element analyses. It should be noted that the optimized geometric parameter are mainly the gap width, the coil width, the piston radius and the flange thickness (Nguyen et al. [20]). Also the input current and diameter of coil wire were included as the design parameters to optimize the configuration of an MR damper based on the Taguchi experimental approaches (Parlak et al. [17]).

However, the flow channels of all these MR damper mentioned above were straight, which hindered the maximum dynamic range to some extent. This problem might be deteriorated especially for a multi-coil MR damper which was first proposed by Spencer et al [24] to increase the total damping force for a seismic protection system. To maintain a large dynamic range while keeping the off-state damper force reasonably low (Singh et al. [13]), a new multi-coil MR damper with variable resistance gap (VRG-MMD) was proposed in this study. Therefore, the design variables (DVs) including each flange thickness and radius should be optimized individually. It is noted that the resistance gap should be larger than 1[mm] in order to avoid the risk of valve blocking. Furthermore, the optimal design of the VRG-MMD was performed via multi-physics finite element method which analyzed the magnetic field and the MR fluid flow simultaneously. It is expected that the new optimal design can significantly improve the overall performance of the VRG-MMD. Subsequently, a comparison between the VRG-MMD and the typical multi-coil MR damper (T-MMD) subjected to sinusoidal and triangle displacement excitations was carried out in terms of the damping force and dynamic range.

2. Design of a MR damper with a variable resistance gap

2.1 Structure of multi-coil MR damper with a variable resistance gap

Compared to a single-coil MR damper, the MR damper with multi-stage EMs were designed to increase the maximum resistance force by elongating the gap (Figure 1a). However, the elongated gap decreases the dynamic ratio to some extent. Therefore, in this study, a new multi-coil MR damper with a variable gap was proposed to enlarge the maximum damping force as well as the dynamic ratio.

Figure 1b shows the structure of the initial proposed multi-coil MR damper which is abbreviated to VRG-MMD in the following sections. Please also note that the typical multi-coil MR damper is abbreviated to T-MMD as well. The VRG-MMD consists of out cylinder, MR fluid, piston head, piston rod and multi-stage EMs which develop individual magnetic flux as shown in figure 1. The end covers and seal rings are not shown in the schematic configuration. The VRG-MMD is designed to be double-ended so that it is not necessary to balance the fluid volume change during the motion of the piston inside the hydraulic cylinder. The coil wires were wounded on each spool of the piston head and protruded out through a hole in the piston body. The surface of the piston head was designed with a slope; this means the thickness of the resistance gap is changing when the MR fluid flows. To guarantee the homogenous distribution of the magnetic flux density among the effective areas, the surface of the magnetic poles remain flat.

However, at sufficiently high flow rate, the liquid is most likely to cavitate in the throat where the velocity is the highest and the pressure is the lowest. So that the vapor bubbles are formed and grow as a consequence of rapid pressure reduction in some regions of the flow. The reconversion of the vapor to liquid leads to a powerful micro-jet of liquid being directed towards the solid surface. This has been known to cause pitting of the piston surface (erosion). The bubbles collapse as they are swept downstream into the high-pressure regions near the end of the stroke, giving lots of noise, unexpected vibrations and extreme harshness. To prevent the occurrence of low pressures, a non-magnetic tapered filler as shown in figure 2 was designed to avoid the cavitation by slowly decreasing the local pressure. For simplification, the cross-section area of the filler is required to compensate the cross-section of piston head for forming a rectangle cross-section, i.e., $S_1 = S_2$ .Therefore, the angle θ of the filler can be calculated as:

$$\theta = \arctan(\frac{Max\{R_{pi}\}\times L_p - (\sum_{i=1}^{n}[R_{pi}\times L_{pi}] + \sum_{j=1}^{m}[\frac{1}{2}(R_{pj}+R_{pj+1})\times L_c])}{1/2(R_{pn}-R_r)^2}) \tag{1}$$

A detailed multi-coil VRG-MMD is shown in figure 2 and the key geometric parameters are as follows:

- R_r radius of the piston rod
- R_{in} radius of the inner cylinder
- R_{oc} radius of the out cylinder
- R_{pi} radius of the magnetic poles ($i = 1, \ldots, 5$)

- L_{pi} length of the magnetic poles
- L_p total length of the piston head
- W_c width of the each EM
- L_c length of the each EM

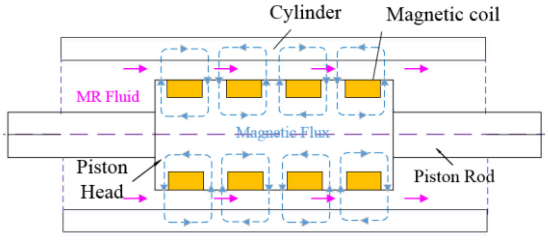

(a) Typical multi-coil MR damper (T-MMD)

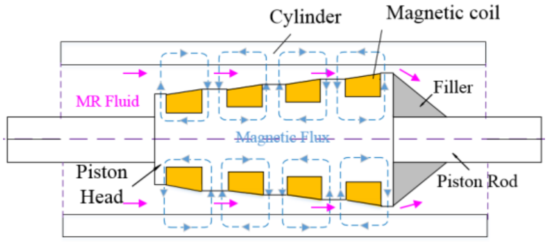

(b) Proposed multi-coil MR damper with a variable resistance gap (VRG-MMD)

Fig 1 Schematic configuration of a double-ended MR damper with four EMs

The initial geometric parameters of the VRG-MMD is shown in table 1 which is determined based on the previous work (zheng et al. [25]). It can be seen that the angle θ is proportional to the thickness summary of the five effective resistance gaps as shown in Equation (1). So the maximum thickness of the effective resistance gaps should be less than 3mm to miniaturize the filler. Once the thickness of the resistance gap is determined, a pressure drop between the inlet and outlet ports of the resistance gap can be estimated when the MR fluid flows through the annular gap. Moreover, by applying exciting currents to the EMs, closed loop paths containing magnetic flux are generated among the piston head, MR fluid and out cylinder; thus additional pressure drop is produced due to the MR effect and therefore the total pressure drop can be controlled.

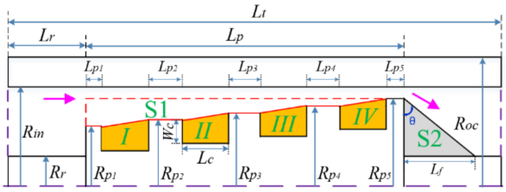

Fig 2 Key geometric parameters of the VRG-MMD

Table 1 Initial geometric parameters of the VRG-MMD [mm]

$\boldsymbol{R_r}$	9	$\boldsymbol{R_{p3}}$	18	$\boldsymbol{L_{p1}}$	5	$\boldsymbol{W_c}$	8.5
$\boldsymbol{R_{in}}$	20	R_{p4}	18.5	L_{p2}	10	L_c	40
$\boldsymbol{R_{oc}}$	28	R_{p5}	19	L_{p3}	10	L_r	30
$\boldsymbol{R_{p1}}$	17	L_p	200	L_{p4}	10	θ	76°
$\boldsymbol{R_{p2}}$	17.5	L_t	300	L_{p5}	5		

2.2 Magnetic field analysis of the VRG-MMD

2.2.1 Magnetic flux density of the MR fluid

In terms of two or more magnetic fields, a magnetic system should be tailored to maximize the control efficiency upon different regions of the resistance gap (Güth Dirk, et al. [26]). An essential requirement is that neighboring components of the magnetic system should be opposite in its polarity to realize a minimum cancellation of the net magnetic flux distribution in the annular gap. Therefore, the directions of the exciting currents applied to the neighbor electromagnets (EMs) should be opposite, as shown in figure 3(a). The magnetic system can be regarded as a simplified system, consisting of five magnetic yokes, four EMs and the resistance gap with its five active and four inactive regions. For simplified analysis of the magnetic field, the magnetic circuit is represented by a simplified magnetic equivalent circuit shown in figure 3(b). To further illustrate, the symbols are adopted to represent the components of the magnetic equivalent circuit. The four EMs are labeled as external voltage sources, which generate the magnetomotive forces ϑ_{CI}, ϑ_{CII}, ϑ_{CIII}, ϑ_{CIV} respectively. The five active regions of MR fluid are represented by constant resistors $R_{m,C1}$, $R_{m,C2}$, $R_{m,C3}$, $R_{m,C4}$ and $R_{m,C5}$, respectively. Please note that the magnetic core losses (i.e. hysteresis loss and eddy current loss) are not considered in the schematic diagram for the desired qualitative analysis.

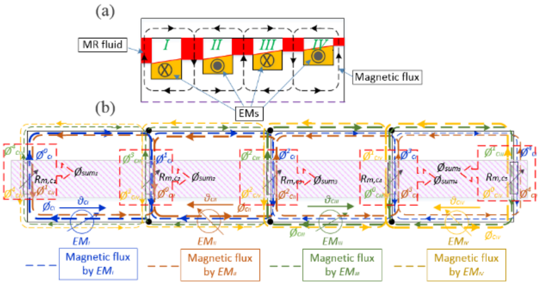

Fig 3 Magnetic system of the VRG-MMD (a) magnetic flux (b) corresponding magnetic equivalent circuit

As explained previously, each of the EMs can be applied with the exciting current individually. In other words, when only one EM, for example, EM_{II}, generates the magnetomotive force, ϑ_{CII}, the magnetic flux passes each of the active MR fluid region with $Ø^1_{cII}$, $Ø^0_{cII}$, $Ø^2_{cII}$, $Ø^3_{cII}$ and $Ø^4_{cII}$, respectively. However, when two or more current-carrying EMs generate the magnetomotive forces, the resultant magnetic flux which pass through each active gap can be understood as vector operations of the magnetic flux generated by each voltage source. Therefore, the resultant magnetic flux passes through each active gap can be expressed by:

$$\begin{bmatrix} Ø_{sum,1} \\ Ø_{sum,2} \\ Ø_{sum,3} \\ Ø_{sum,4} \\ Ø_{sum,5} \end{bmatrix} = \begin{Bmatrix} |Ø^0_{cI} - Ø^1_{cII} + Ø^4_{cIII} - Ø^4_{cIV}| \\ |-Ø^1_{cI} - Ø^0_{cII} + Ø^3_{cIII} - Ø^3_{cIV}| \\ |-Ø^2_{cI} + Ø^2_{cII} + Ø^2_{cIII} - Ø^2_{cIV}| \\ |-Ø^3_{cI} + Ø^3_{cII} - Ø^0_{cIII} - Ø^1_{cIV}| \\ |-Ø^4_{cI} + Ø^4_{cII} - Ø^1_{cIII} - Ø^0_{cIV}| \end{Bmatrix} \quad (2)$$

$$For\ \ EM_{I,IV}, \qquad Ø_{cI,IV} = Ø^0_{cI,IV} = Ø^1_{cI,IV} + Ø^2_{cI,IV} + Ø^3_{cI,IV} + Ø^4_{cI,IV}$$

$$For\ \ EM_{II,III}, \qquad Ø_{cII,III} = Ø^0_{cII,III} + Ø^1_{cII,III} = Ø^2_{cII,III} + Ø^3_{cII,III} + Ø^4_{cII,III}$$

Since the yield stress of the MR fluid depends on the applied magnetic field, it is important to analyze the detailed distribution of the magnetic flux density across the active regions. As mentioned before, two methods have been employed to analyze the magnetic circuit to approximately evaluate the magnetic flux density in the fluid region: analytical approach (Nguyen et al. [20]; Nguyen et al. [21]) and numerical approach (Nguyen et al. [14]; Nguyen et al. [15]; Hadadian et al. [27]). Due to many simplified assumptions, the accuracy of the magnetic field distribution using analytical solutions might be far away from expected (Hadadian et al. [27]). However, the numerical approach based on the finite element method gains more popularity in the literatures.

In this section, a finite element model is constructed to examine and analyze the average magnetic field intensity and magnetic flux density along the annular gap. The materials for the piston and cylinder are AISI 1018 steel and MRF-140CG from Lord Corporation were used. Since the geometry of the VRG-MMD structure is axisymmetric, a two dimensional axisymmetric model has been adopted and to reduce the computation cost as shown in figure 3(a). In the FEM solutions, it is obvious that the magnetic field intensity and the magnetic flux density are not constant both along the radial and axial directions (Nguyen et al. [28]). It was also found that the effective length of the active gap is definitely longer than the geometric length of the magnetic pole. Therefore, the magnetic flux and the average magnetic flux density across the active regions can be determined as follows:

$$\underset{i=1,\dots,n}{Ø\ _{sum,i}} = \frac{\pi(R_{in}+R_{pi})}{S^*_{pi}} \int_0^{S^*_{pi}} B_{mr,i}(s)ds \quad (3)$$

$$\underset{i=1,\dots,n}{\bar{B}\ _{mr,i}} = \frac{1}{S^*_{pi}} \int_0^{S^*_{pi}} B_{mr,i}(s)ds \quad (4)$$

where $B_{mr,i}(s)$ is the magnetic flux density at each nodal point on the ^{i}th defined path along the active region where magnetic flux passes. S^*_{pi} is the effective region of the ^{i}th magnetic poles ($S^*_{pi} = \xi S_{pi}$).

Figure 4 shows the magnetic flux density of each magnetic pole on the fluid region with four exciting currents increasing synchronously from 0.5A to 2A by a step of 0.5A. Obviously, the magnetic flux density of the MR fluid increases with the increment of exciting currents and the decrement of the resistance gap thickness. It is inevitable that the distribution of the magnetic flux density in the active region is inhomogeneous. This is because that the magnetic flux always concentrates on the two corner points of the magnetic poles when passing through the resistance gap. So it is necessary to evaluate the average magnetic flux density of MR fluid to achieve an accurate result, as indicated by Equation (4). Further observation indicates that by adjusting the gap thickness from 3mm to 1mm, the average magnetic flux density of the MR fluid varies from 0.8T to 1.3T when each EM is applied with an exciting current of 2A. Thus, the gap thickness is significantly sensitive to the magnetic flux density as well as the fluid flow, which will be explained in the following sections.

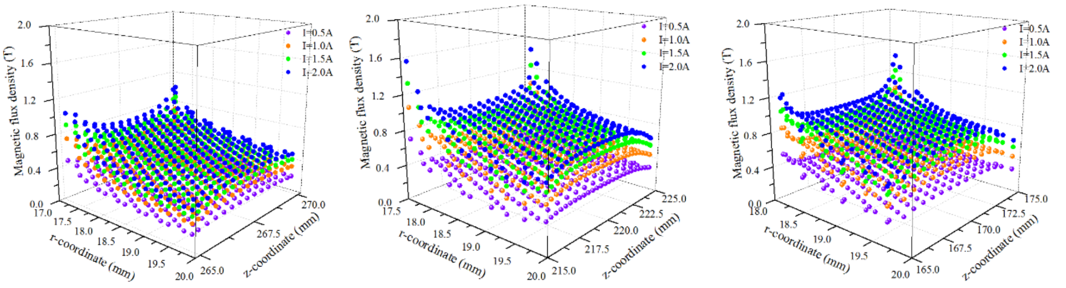

(a) Magnetic pole1 (b) Magnetic pole2 (c) Magnetic pole3

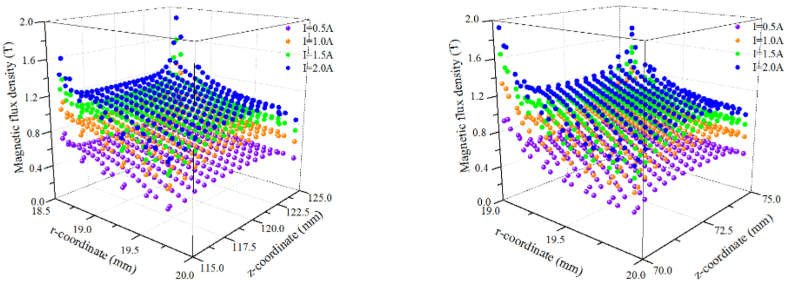

(c) Magnetic pole4 (d) Magnetic pole5

Fig 4 Magnetic flux density of active fluid region (pole1-5)

2.2.2 *Inductive time constant and control energy*

For the real-time control systems, it is desirable that the MR damper has fast time response. Thus, the inductive time constant of the MR damper is an important index and it should be implemented into the design for practical applications. The inductive time constant is defined as time needed for current flowing in an inductive circuit to reach its 63.2% of its steady-state value and it can be expressed as (Nguyen et al. [29]):

$$T = max_{j=1,\dots,m}\left\{\frac{N_c\emptyset_c}{IR_w}\right\}_j \tag{5}$$

Correspondingly, the power consumption of the EMs can be calculated as follows:

$$\underset{j=1,\dots,m}{P}{}_{w,j} = \{I^2R_w\}_j \tag{6}$$

In the above, I_j is the exciting current applied to the jth EM and R_w is the resistance and N_{cj} is the turns of the jth EM, $N_{cj} = A_{cj}/(\epsilon \times A_w)$. A_{cj} and A_w are the cross-sectional areas of the jth EM and copper wire respectively. Therefore, equations (5) and (6) can be rewritten as:

$$T = max_{j=1,\ldots,m}\left\{\frac{\emptyset_{cj}D_{cw}^2}{2I_j\tilde{r}\left(3R_{pj}+R_{pj+1}-2w_c\right)}\right\} \qquad (7)$$

$$\underset{j=1,\ldots,m}{P_{w,j}} = \left\{\frac{4L_c(2w_c+R_{pj+1}-R_{pj})(3R_{pj}+R_{pj+1}-2w_c)\tilde{r}I_j^2}{\epsilon\pi D_{cw}^4}\right\} \qquad (8)$$

where D_{cw} and $\tilde{r}$ are the diameter and resistivity of the copper wire respectively, $D_{cw} = 0.56[mm]$, $\tilde{r} = 1.726 \times 10^{-8}[\Omega m]$ and ϵ is a coefficient for rolling copper wire, $\epsilon = 1.77$.

For the VRG-MMD with the initial geometric parameters, the maximum inductive time constant occurs in the EM_{IV}, as shown in figure 5. Obviously, the inductive time constant decreases as the exciting current increases, as indicated by Equation (7). However, the average inductive time constant of the initial VRG-MMD reaches 200ms, which means that multi-coil MR damper behaves a slower response compared to single-coil MR damper. In other words, the time response should be paid more attention to in terms of the multi-coil MR damper. On the other hand, the maximum power consumption of the control energy occurs in the EM_{IV} as well (figure 6). The total control energy consumed by the EMs is around 30W when each of the EM is applied with an exciting current of 2A.

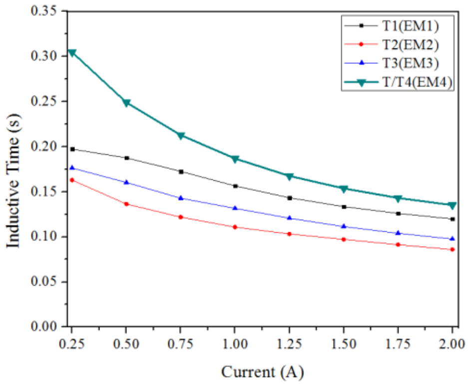

Fig 5 Inductive time constant

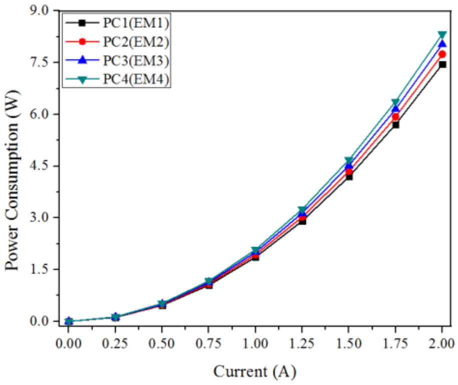

Fig 6 Power consumption (control energy)

2.3 Fluid dynamic analysis of the VRG-MMD

2.3.1 Damping force

As shown in figure 1(b), the VRG-MMD is divided into upper and lower chambers, both of which are fully filled with the MR fluid (MRF-140CG). As the piston moves under external excitations, the MR fluid flows from one chamber to the other through the variable annular gap. Here, the frictional force of the VRG-MMD is neglected and the total damping force can be expressed as follows assuming a quasi-static behavior.

$$F_d = P_u\tilde{A}_{pu} - P_l\tilde{A}_{pl}cos\theta \qquad (9)$$

By substituting the effective upper and lower effective piston areas ($\tilde{A}_{pu}$ and $\tilde{A}_{pl}$) with the geometric parameters shown in figure 2, Equation (9) can be rewritten as follows:

$$F_d = P_u\pi\left(R_{p1}^2 - R_r^2\right) - P_l\pi(R_{p5}^2 - R_r^2)\sqrt{1+\sin^2\theta} \qquad (10)$$

$$|P_u - P_l| = \Delta P \qquad (11)$$

The damper force was evaluated by the total pressure drop (ΔP) occurring inside the hydraulic cylinder due to the fluid flow which experiences the following phenomena (Singh et al. [13]):

(a) Viscous losses due to friction along the piston

(b) Minor loss due to entrance, exit, sudden/gradual expansion and contraction

(c) MR effect

The pressure drops due to viscous losses (a) and minor losses (b) are proportional to the squared fluid velocity and are given as:

$$\Delta P_\eta = \frac{f_D \rho}{4} \left(\sum_{i=1}^{n} \frac{L_{pi}}{(R_{in} - R_{Pi})} \bar{V}_i^2 + \sum_{j=1}^{m} \frac{L_c}{\left(R_{in} - \left(\frac{R_{pj} + R_{pj+1}}{2} \right) \right)} \bar{V}_j^2 \right) \tag{12}$$

$$\Delta P_m = \frac{\rho}{2} \left(\sum_k K_{m\_k} \bar{V}_{m\_k}^2 \right) \tag{13}$$

where K_{m_k} is the ^{k}th minor loss coefficient along the fluid flow path and $\bar{V}_{m\_k}$ is the corresponding average fluid velocity. These minor loss coefficients are semi-empirical and adopted from hydraulic handbooks (White [30]; Idelchik [31]). $\bar{V}_i$ and $\bar{V}_j$ are the average fluid velocities in the active and inactive fluid regions along the resistance gap and are given as:

$$\bar{V}_i = \frac{R_{in}^2 - R_r^2}{R_{in}^2 - R_{pi}^2} \bar{V}_p; \;\; \bar{V}_j = \frac{R_{in}^2 - R_r^2}{R_{in}^2 - \left(\frac{R_{pj} + R_{pj+1}}{2} \right)^2} \bar{V}_p \tag{14}$$

where $\bar{V}_p$ is the average input piston velocity.

The Darcy friction factor, f_D , was determined by the types of flow and was dependent on Reynolds number, Re.

$$f_D = \frac{64}{Re} \qquad if \;\; Re < 2300 \tag{15}$$

$$\frac{1}{f_D^{0.5}} = -2 \log\left(\frac{\frac{e}{\tilde{d}_{pc}}}{7.4} + \frac{2.51}{Re f_D^{0.5}} \right) if \;\; Re > 2300 \tag{16}$$

$$\text{with } Re = \frac{2 \rho \bar{V} \tilde{d}_{pc}}{\eta}$$

where $\tilde{d}_{pc}$ is the thickness of the variable resistance gap. e is the average pipe wall roughness; ρ is the fluid density and η is the fluid viscosity.

The field-dependent pressure drop due to MR effect (c), with a m-stage coil configuration was generally calculated as m times of each field-dependent pressure drop with a single coil configuration (Singh et al. [13]). However, as explained in section 2.2, the phenomena of superposition and cancellation occur in the five magnetic poles when exciting currents are applied to the EMs individually. Therefore, to improve the accuracy of the pressure drop due to MR effect, the field-dependent pressure drop with m-stage coil configuration is evaluated by:

$$\Delta P_\tau = 2 \sum_{i=1}^{n} \frac{L_{pi}^* \tau_y^i}{(R_{in} - R_{pi})} \tag{17}$$

The field-induced yield stress of the MR fluid as a function of the applied magnetic field intensity (H_{mr}) can be approximately expressed as follows using the least square curve fitting method.

$$\tau_y = k_1 H_{mr}^4 + k_2 H_{mr}^3 + k_3 H_{mr}^2 + k_4 H_{mr} + k_5 \tag{18}$$

where $k = [9.2E-9 \quad -5.4E-6 \quad 2.83E-4 \quad 0.31 \quad 0.015]$, the units of the τ_y and H_{mr} are kPa and kA/m, respectively.

2.3.2 *Dynamic range*

A key performance index is the dynamic range, which is defined as the ratio of the total damper force to the off-state damping force and a large value of the dynamic range is desirable.

$$\lambda = 1 + \frac{F_\tau}{F_m + F_\eta} \tag{19}$$

As explained before, the numerical approach was adopted to compute the off-state damping force under external excitations using FEM software COMSOL 4.4. For computational time reduction, the computational domain was reduced to a two dimensional (2D) axisymmetric fluid model. This model was meshed with quadrilateral elements by controlling the element number of 191,880 and average element quality of 0.8748. Please note that the fluid region was meshed separately with very small element size to obtain accurate velocity profiles. The boundary conditions applied to the fluid model are corresponding to: (i) no-slip for the fluids at the inner cylinders and piston walls; (ii) an inlet at the initial end and an opening at the end of the fluid region with a relative pressure. In this study, the MR fluid was assumed to be incompressible, while the flow was considered to be laminar. The enhanced wall treatment was used to predict the off-state pressure drop between the upstream and downstream. Quasi-steady simulations were conducted for input piston velocities varying from 0.25-1 m/s.

Figure 5 shows the results of pressure contours obtained from the numerical simulation. The initial viscosity of the MRF-140CG is η=0.28 [Pa*s] and its density is ρ =3540 [kg/m^3] at room temperature. According to the equation (9), the off-state damping force is then obtained based on the viscous pressure drops shown in figure 5. Further investigation shows that the gap thickness is significantly sensitive to the local pressure drop as mentioned before.

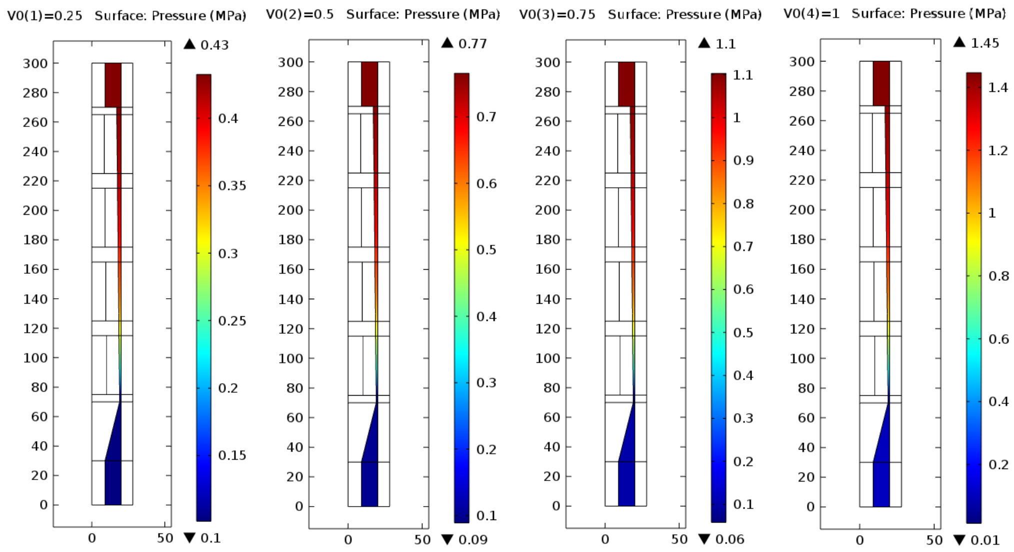

(a) $\bar{V}_p = 0.25[m/s]$ (b) $\bar{V}_p = 0.5[m/s]$ (c) $\bar{V}_p = 0.75[m/s]$ (d) $\bar{V}_p = 1.0[m/s]$

Fig 7 Off-field fluid pressure drop

The controlled pressure drop due to yield stress was evaluated by equation (17) and (18) using the magnetic FE simulation (B-field) obtained in section 2.2. Some design parameters are sensitive to the field-dependent pressure drop: exciting current, number of coil wire turns, radius and length of each magnetic pole (R_{pi} and L_{pi}). These analyses were conducted with the exciting current varying from 0.25-2.0[A] and each local pressure drop due to yield stress was shown in figure 8. As can be seen, the fourth magnetic pole generates the maximum field-dependent pressure drop and the first magnetic pole obtains the minima. This means that the length elongation of the magnetic pole (L_{pi}) increases the field-dependent pressure drop and similarly, the radius increment of the magnetic pole (R_{pi}) also increases the field-dependent pressure drop. However, to low the off-state damping force, both the length and radius of the magnetic pole should be in a reasonable range. Therefore, the dynamic range as shown in equation (19) is an important index evaluating the performance of the VRG-MMD. Obviously, the dynamic range λ is reversely proportional to the piston velocity as indicated in figure 9. The maximum dynamic range λ reaches 11.25 with each input current I_j=2.0[A], and an input velocity $\bar{V}_p$=0.25[m/s].

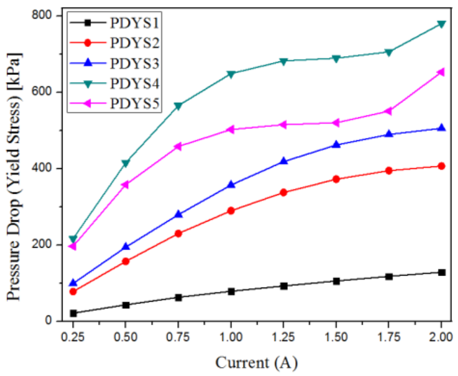

Fig 8 Local pressure drop due to yield stress

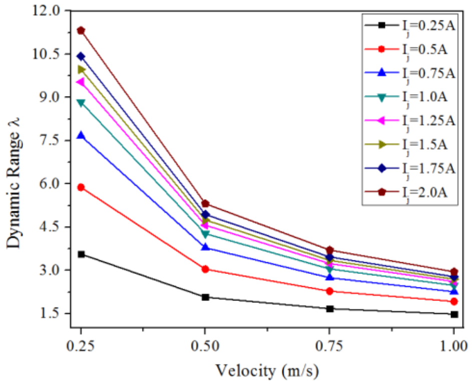

Fig 9 Dynamic range

3. Optimization of the VRG-MMD

3.1 Objective function

In this section, the objective of the optimization problem obtain the optimal geometry of the VRG-MMD via a commercial finite element based optimization tool. It is clear that high damping is desirable to reduce vibration quickly, and on the contrary, a low off-field damping force is required to increase the controllability. It should be also noted that the adaptability to different situations (impulsive load, etc) is significantly affected by the inductive time constant. Therefore, a multi-objective function must be established to evaluate the overall performances of the VRG-MMD (Nguyen and Choi [20]; Hadadian et al. [27]). Thus, a non-dimensional multi-objective function including the concerned performance indices (total damping force, dynamic range, and inductive time constant) is expressed as follows:

$$f = \alpha \frac{F_{dr}}{F_d} + \beta \frac{\lambda_r}{\lambda} + \gamma \frac{T}{T_r} \tag{20}$$

$$\alpha + \beta + \gamma = 1 \tag{21}$$

where F_d, λ, and T are the total damping force, dynamic range and the inductive time constant, respectively. The parameters F_{dr}, λ_r, and T_r are the references which are evaluated based on the initial geometric parameters shown in table 1. Moreover, the coefficients α, β, and γ are the respective weighting factors which aim to combine multiple objective functions into a single objective function. The value of the weighting factors are determined according to the requirements of the specific applications (Hadadian et al. [27]).

For a given damper volume (known values of R_{in} and L_p), the geometric parameters (the coil width W_c, the pole radius R_{pi} and the pole length L_{pi}, etc) affecting the overall performance of the VRG-MMD significantly are selected as the design variables (DVs). During the optimization process, real-time re-meshing has been enabled in an effort to obtain accurate results. After solving the magnetic circuit of the VRG-MMD by FE analysis, the average magnetic flux density ($\bar{B}_{mr,i}$) in ^{i}th region and the inductive time constant are calculated by equation (4) and (5), respectively. The yield stress of each active region is then estimated from the polynomial approximation as shown in equation (18). Once the yield stress of each active region is obtained, the damping force and dynamic range can be obtained combing the equations (9)-(19). The multi-objective function developed in equation (20) is solved using the Bound Optimization BY Quadratic Approximation (BOBYQA), which is a powerful derivative-free algorithm for solving bound constrained optimization problems (Powell [32]). A general outline of the steps to optimize the DVs of the VRG-MMD using the BOBYQA algorithm is shown in figure 10.

Before the execution of the optimization, the DVs and state variables with their limits and tolerances as well as the convergence criteria must be specified. It is known that the magnetic flux density is proportional to the exciting current. Without losing any generality, the exciting current is set as $I_j = 1[A]$ and the input piston velocity as $\overline{V}_p = 0.5 \ [m/s]$. For a given damper volume ($R_{in} = 20[mm]$ and $L_p = 200[mm]$), the design space of the selected DVs are limited by specifying the lower and upper tolerances:

$$\begin{gathered} 5[mm] \le W_c \le 10[mm] \qquad (23) \\ 17[mm] \le R_{pi} \le 19[mm] \\ 5[mm] \le L_{pi} \le 20[mm] \end{gathered}$$

It is noted that the maximum angle of the filler θ should be less than 80° for the damper compactness. Therefore, we can mathematically formulate the multi-objective optimization problem as:

$$Minimize \quad f(W_c, R_{pi}, L_{pi}) = \alpha \frac{F_{dr}}{F_d} + \beta \frac{\lambda_r}{\lambda} + \gamma \frac{T}{T_r}$$

(24)

$$Subject\ to \qquad 0° < \theta \le 80°$$

So far, there is no clear regulation for selecting the weighting factors. As a result, different combinations of the weighting factors which are empirically specified definitely have great impact on the damping capacity and consequently achievable performances (Zhu et al. [33]).

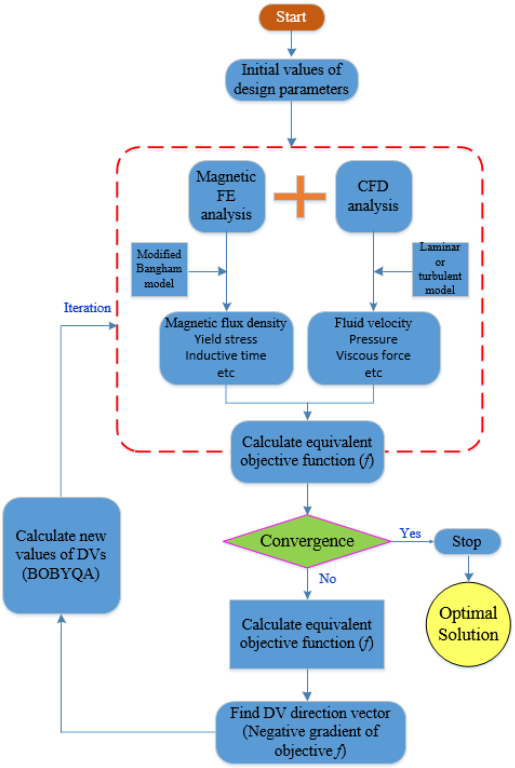

Fig10 Flow steps for optimal solutions

3.2 Results and discussion

After executing the optimization procedure developed in section 3.1, the optimal solutions are summarized in Table 2-7. It can be seen that the performance of the VRG-MMD with the optimum configurations has been significantly improved in comparison with those in reference. As expected, the optimum pole lengths (L_{p2},L_{p3}, L_{p4}) turn out to be different from each other. However, current literatures usually design the pole length as $L_{p2} = \cdots = L_{pm} = 2L_{p1} = 2L_{pm+1}$ for an m-stage EMs (Nguyen et al. [14], Singh et al [13]). In fact, the magnetic field is significantly affected by the magnetic pole length L_{pi}. By increasing the length of L_{pi}, more MR fluid are exposed under magnetic field and consequently larger yield stress can be generated. Once each pole radius R_{pi} can be adjusted individually, the average magnetic flux density of each active region differs a lot. But more attention should be paid to the sensitivity of the off-state damping force to the alteration of the pole radius R_{pi}. This is because large pole radius

R_{pi} (small gap thickness) can dramatically increase the off-state damping force. Furthermore, as explained before, there are superposition and cancellation of the magnetic flux upon the magnetic poles when each EMs are applied with the exciting currents. Therefore, it is extremely expected to have the pole radius R_{pi} and pole lengths L_{pi} varied according to the specified multi-objective function.

Table 2 shows the optimal configuration of the MR damper when the weighting factors are selected as $\alpha = 1$, $\beta = 0$, $\gamma = 0$. The optimal values of the design variables (DVs) yield to $W_c = 10$, $R_{p1} = 19$, $R_{p2} = 17.739$, $R_{p3} = 19$, $R_{p4} = 19$, $R_{p4} = 19$, $L_{p1} = 7.7942$, $L_{p2} = 10.387$, $L_{p3} = 10.399$, $L_{p4} = 15.005$, $L_{p5} = 7.5596$, and $\theta = 16°$. It is indicated that all the pole radius R_{pi} except R_{p2} take their upper limit value of 19[mm] and coil width W_c takes its upper limit value of 10[mm]. This is completely in agreement with the physical perception of the problem.

Table 3 shows the optimal configuration of the MR damper when the weighting factors are selected as $\alpha = 0$, $\beta = 1$, $\gamma = 0$. It can be concluded that two approaches are employed by BOBYQA for maximizing the dynamic range: reducing the off-state force by decreasing the pole radius R_{pi} and increasing the field-dependent force by elongating the pole length L_{pi}. At the optimal dynamic range, the optimal objective was found to be almost 72% increment compared with the reference value.

Table 4 shows the optimal configuration of the MR damper when the weighting factors are selected as $\alpha = 0$, $\beta = 0$, $\gamma = 1$. The inductive time of the multi-coil damper is defined as the maximum inductive time generated by each EM. The optimal solution shows that the inductive time of the VRG-MMD can be reduced by decreasing the pole length $L_{p\mathrm{i}}$ and coil width W_c, as indicated by equation (7).

It is noteworthy that the values of the weighting factors are selected depending to each specific damping system. If the MR damper is used for seismic protection against earthquake, large total damping force is required and a large value of α should be chosen in the multi-objective function. If the MR damper is used to improve the ride comfort of a vehicle suspension system, small off-state damping force and a large value of β should be chosen. If the MR damper is used for tracking desired damping profile under impact load, fast time response is preferred and consequently a large value of γ should be chosen. Tables 5-7 show the optimal configurations of the MR dampers when the weighting factors are selected as $\alpha = 0.5$, $\beta = 0.2$, $\gamma = 0.3$; $\alpha = 1/3$, $\beta = 1/3$, $\gamma = 1/3$; $\alpha = 0.2$, $\beta = 0.4$, $\gamma = 0.4$, respectively. The optimal results reveal that the overall performance of the VRG-MMD (damping force, dynamic range and inductive time) can be significantly improved. By changing the values of weighting factors, a new optimal solution of the VRG-MMD can be obtained. Its performance will be dominated by the term with a larger value of weighting factor. Therefore, the designers should have a good knowledge about the specific requirements of different applications. In such a way, suitable values of the weighting functions can be chosen for the specific optimization design of a multi-coil MR damper. In addition, it is noted that the damping force and dynamic range will increase, the inductive time will decrease by increasing the applied exciting currents to the EMs. Thus, the performance of the VRG-MMD can be further improved by setting the exciting currents as I_j=2 or 2.5[A].

Table 2. Optimal configuration of the VRG-MMD: $\alpha = 1,\ \beta = 0,\ \gamma = 0.$

Design variables (mm)						Performance index	
Initial	Optimum (BOBYQA)	Initial	Optimum (BOBYQA)	Initial	Optimum (BOBYQA)	Initial	Optimum (BOBYQA)
$W_c = 8.5$	$W_c = 10$	$R_{p4} = 18.5$	$R_{p4} = 19$	$L_{p3} = 10$	$L_{p3} = 10.399$	$F_{dr} = 1605[N]$	$F_d = 5600[N]$
$R_{p1} = 17$	$R_{p1} = 19$	$R_{p5} = 19$	$R_{p5} = 19$	$L_{p4} = 10$	$L_{p4} = 15.005$	$\lambda_r = 4.3$	$\lambda = 3.193$
$R_{p2} = 17.5$	$R_{p2} = 17.739$	$L_{p1} = 5$	$L_{p1} = 7.7942$	$L_{p5} = 5$	$L_{p5} = 7.5596$	$T_r = 190[ms]$	$T = 270[ms]$
$R_{p3} = 18$	$R_{p3} = 19$	$L_{p2} = 10$	$L_{p2} = 10.387$	$\theta = 76°$	$\theta = 16°$	$f = 1$	$f = 0.28659$

Table 3. Optimal configuration of the VRG-MMD: $\alpha = 0,\ \beta = 1,\ \gamma = 0.$

Design parameters (mm)						Performance index	
Initial	Optimum (BOBYQA)	Initial	Optimum (BOBYQA)	Initial	Optimum (BOBYQA)	Initial	Optimum (BOBYQA)
$W_c = 8.5$	$W_c = 9.7812$	$R_{p4} = 18.5$	$R_{p4} = 17.035$	$L_{p3} = 10$	$L_{p3} = 19.646$	$F_{dr} = 1605[N]$	$F_d = 922[N]$
$R_{p1} = 17$	$R_{p1} = 17$	$R_{p5} = 19$	$R_{p5} = 18.395$	$L_{p4} = 10$	$L_{p4} = 19.606$	$\lambda_r = 4.3$	$\lambda = 15$
$R_{p2} = 17.5$	$R_{p2} = 17.089$	$L_{p1} = 5$	$L_{p1} = 18.475$	$L_{p5} = 5$	$L_{p5} = 5$	$T_r = 190[ms]$	$T = 234[ms]$
$R_{p3} = 18$	$R_{p3} = 17.032$	$L_{p2} = 10$	$L_{p2} = 19.684$	$\theta = 76°$	$\theta = 54.3°$	$f = 1$	$f = 0.27855$

Table 4. Optimal configuration of the VRG-MMD: $\alpha = 0,\ \beta = 0,\ \gamma = 1.$

Design parameters (mm)						Performance index	
Initial	Optimum (BOBYQA)	Initial	Optimum (BOBYQA)	Initial	Optimum (BOBYQA)	Initial	Optimum (BOBYQA)
$W_c = 8.5$	$W_c = 5.1849$	$R_{p4} = 18.5$	$R_{p4} = 17.988$	$L_{p3} = 10$	$L_{p3} = 6.7418$	$F_{dr} = 1605[N]$	$F_d = 760[N]$
$R_{p1} = 17$	$R_{p1} = 17.461$	$R_{p5} = 19$	$R_{p5} = 17.425$	$L_{p4} = 10$	$L_{p4} = 6.7308$	$\lambda_r = 4.3$	$\lambda = 3.17$
$R_{p2} = 17.5$	$R_{p2} = 17.5$	$L_{p1} = 5$	$L_{p1} = 5.0042$	$L_{p5} = 5$	$L_{p5} = 5$	$T_r = 190[ms]$	$T = 86[ms]$
$R_{p3} = 18$	$R_{p3} = 18.595$	$L_{p2} = 10$	$L_{p2} = 5.1965$	$\theta = 76°$	$\theta = 53°$	$f = 1$	$f = 0.45184$

Table 5. Optimal configuration of the VRG-MMD: $\alpha = 0.5,\ \beta = 0.2,\ \gamma = 0.3.$

Design parameters (mm)						Performance index	
Initial	Optimum (BOBYQA)	Initial	Optimum (BOBYQA)	Initial	Optimum (BOBYQA)	Initial	Optimum (BOBYQA)
$W_c = 8.5$	$W_c = 7.8601$	$R_{p4} = 18.5$	$R_{p4} = 18.426$	$L_{p3} = 10$	$L_{p3} = 16.25$	$F_{dr} = 1605[N]$	$F_d = 3706[N]$
$R_{p1} = 17$	$R_{p1} = 18.967$	$R_{p5} = 19$	$R_{p5} = 19$	$L_{p4} = 10$	$L_{p4} = 16.028$	$\lambda_r = 4.3$	$\lambda = 4.32$
$R_{p2} = 17.5$	$R_{p2} = 17.208$	$L_{p1} = 5$	$L_{p1} = 8.011$	$L_{p5} = 5$	$L_{p5} = 5.6144$	$T_r = 190[ms]$	$T = 183.6[ms]$
$R_{p3} = 18$	$R_{p3} = 18.724$	$L_{p2} = 10$	$L_{p2} = 17.97$	$\theta = 76°$	$\theta = 50.66°$	$f = 1$	$f = 0.70105$

Table 6. Optimal configuration of the VRG-MMD: $\alpha = 1/3,\ \beta = 1/3,\ \gamma = 1/3.$

Design parameters (mm)						Performance index	
Initial	Optimum (BOBYQA)	Initial	Optimum (BOBYQA)	Initial	Optimum (BOBYQA)	Initial	Optimum (BOBYQA)
$W_c = 8.5$	$W_c = 8.2559$	$R_{p4} = 18.5$	$R_{p4} = 18.502$	$L_{p3} = 10$	$L_{p3} = 13.901$	$F_{dr} = 1605[N]$	$F_d = 2615[N]$
$R_{p1} = 17$	$R_{p1} = 18.702$	$R_{p5} = 19$	$R_{p5} = 18.446$	$L_{p4} = 10$	$L_{p4} = 10.791$	$\lambda_r = 4.3$	$\lambda = 4.46$

$\boldsymbol{R_{p2}} = \mathbf{17.5}$	$R_{p2} = 17.413$	$L_{p1} = 5$	$L_{p1} = 6.1447$	$L_{p5} = 5$	$L_{p5} = 5.768$	$T_r = 190[ms]$	$T = 164.5[ms]$
$\boldsymbol{R_{p3}} = \mathbf{18}$	$R_{p3} = 18.64$	$L_{p2} = 10$	$L_{p2} = 11.104$	$\theta = 76°$	$\theta = 47.12°$	$f = 1$	$f = 0.80725$

Table 7. Optimal configuration of the VRG-MMD: $\alpha = 0.2,\ \beta = 0.4,\ \gamma = 0.4$.

Design parameters (mm)						Performance index	
Initial	Optimum (BOBYQA)	Initial	Optimum (BOBYQA)	Initial	Optimum (BOBYQA)	Initial	Optimum (BOBYQA)
$\boldsymbol{W_c} = \mathbf{8.5}$	$W_c = 8.0867$	$R_{p4} = 18.5$	$R_{p4} = 17.854$	$L_{p3} = 10$	$L_{p3} = 13.895$	$F_{dr} = 1605[N]$	$F_d = 1746[N]$
$\boldsymbol{R_{p1}} = \mathbf{17}$	$R_{p1} = 18.440$	$R_{p5} = 19$	$R_{p5} = 18.365$	$L_{p4} = 10$	$L_{p4} = 14.799$	$\lambda_r = 4.3$	$\lambda = 6.16$
$\boldsymbol{R_{p2}} = \mathbf{17.5}$	$R_{p2} = 17.179$	$L_{p1} = 5$	$L_{p1} = 6.1725$	$L_{p5} = 5$	$L_{p5} = 5$	$T_r = 190[ms]$	$T = 158.4[ms]$
$\boldsymbol{R_{p3}} = \mathbf{18}$	$R_{p3} = 18.272$	$L_{p2} = 10$	$L_{p2} = 12.666$	$\theta = 76°$	$\theta = 49.45°$	$f = 1$	$f = 0.79016$

4. Performance evaluation of the optimal VRG-MMD

4.1 Damped sinusoidal excitations

To evaluate the dynamic characteristics of the optimized VRG-MMD, the case of $\alpha = 1/3,\ \beta = 1/3,\ \gamma = 1/3$ in previous section has been studied by applying exponentially damped sinusoidal excitation:

$$z(t) = a_0 \sin(2\pi f t)\, e^{-\lambda t} \qquad (25)$$

where a_0 is the amplitude, f is the frequency and λ is the decay constant.

In order to compare with the optimized VRG-MMD, the dynamic characteristics of the T-MMD with geometric parameters $W_c = 8.5$, $L_c = 40$, $R_{p1} = R_{p2} = R_{p3} = R_{p4} = R_{p5} = 18.5$, $L_{p2} = L_{p3} = L_{p4} = 2L_{p1} = 2L_{p5} = 10$ has also been studied. Figure 11 shows the velocity and pressure contour obtained from the CFD analysis when the piston velocity is $\bar{V}_p$ =1[m/s]. It is clearly observed that the fluid forms vortex in the back chamber with sudden extension. In other words, the filler can relatively eliminate the vortex of the fluid by avoiding extremely low pressure regions during the damper compression and extension. Figure 12 shows the off-state damping force under the exponentially damped sinusoidal excitations as shown in equation (25) with the frequency varying from 0.5 to 1.25[Hz]. In a sense, the maximum off-state damping force generated by the optimized VRG-MMD is almost twice that of the T-MMD. However, due to the optimization for the magnetic circuit, the controllable force of the optimized VRG-MMD also improved significantly compared to that of the T-MMD as shown in figure 13. Please note that the Bingham model (Yang et al. [34], Spencer et al. [35]) for the MR fluid was utilized in the simulation and the hysteresis phenomenon due the ferromagnetic hysteresis and fluid friction flow was not considered in this study.

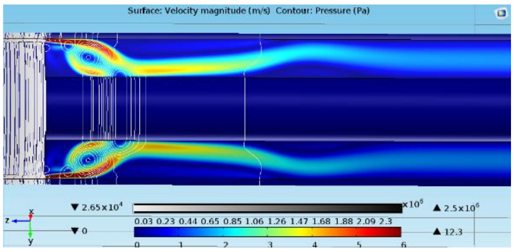

(a)

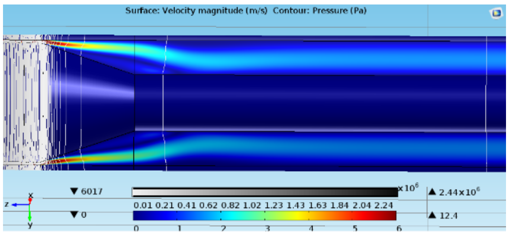

(b)

Fig 11 Velocity and pressure obtained from the CFD
for (a) T-MMD (b) VRG-MMD
(a_0=150[mm], f=1.25[Hz], λ=0)

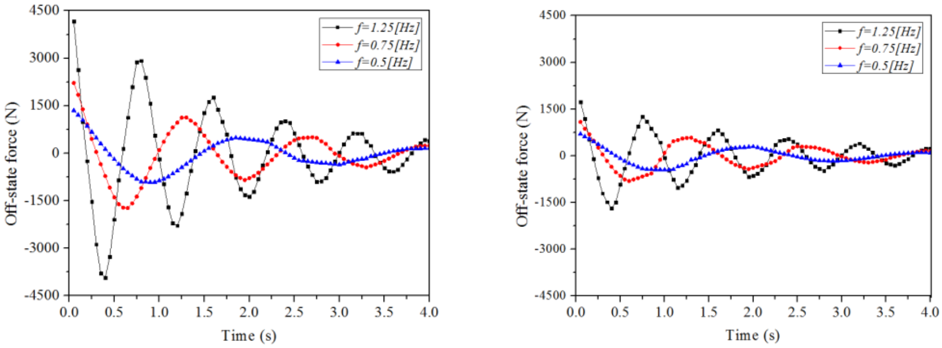

(a) (b)

Fig 12 Off-state force obtained from the CFD for (a) VRG-MMD (b) T-MMD with damped displacement
(a_0=150[mm], λ=0.5)

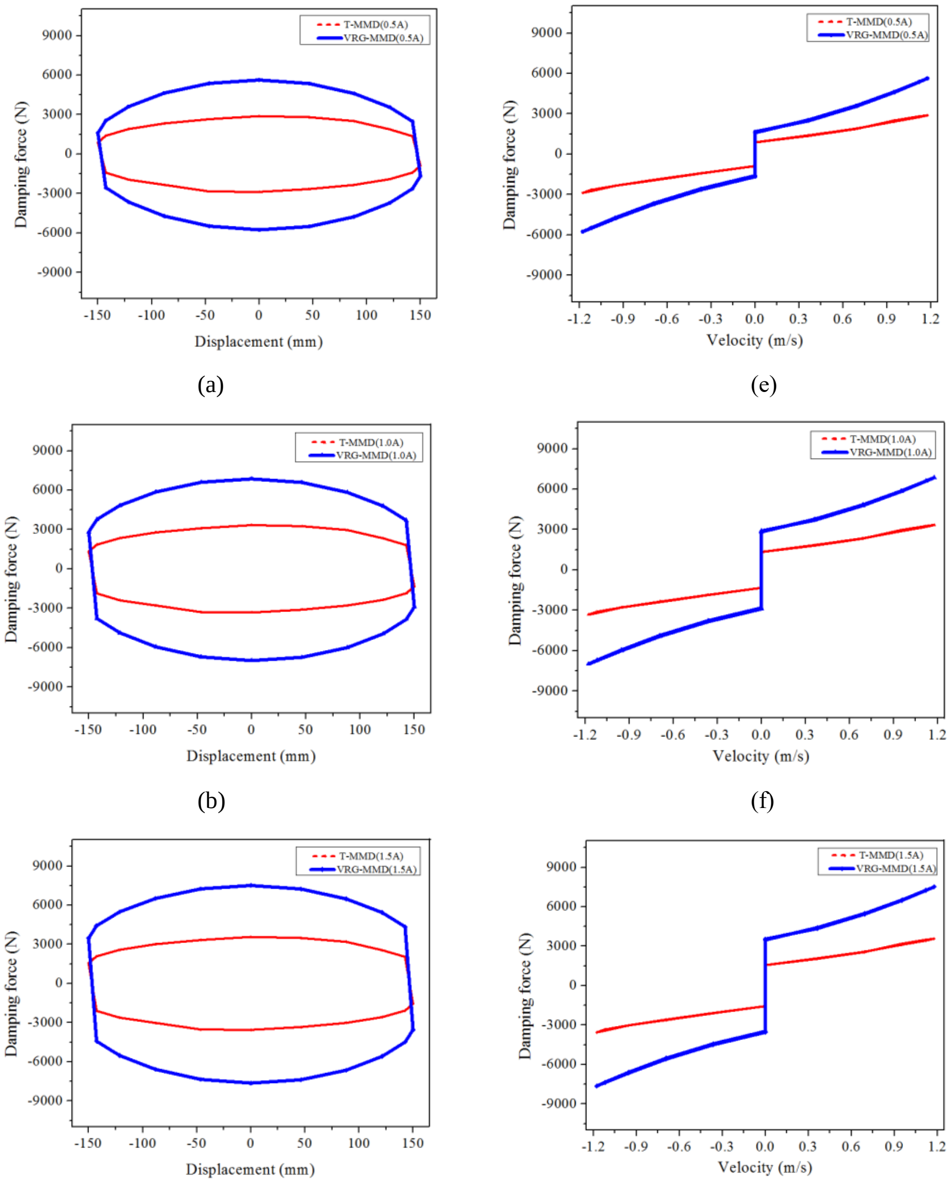

(a) (e)

(b) (f)

(c) (g)

Fig 13 Curves of (a-c) damping force vs. displacement and (e-f) damping force vs. velocity for currents 0.5A, 1A, 1.5A (a_0=150[mm], f=1.25[Hz], λ=0)

4.2 Triangle excitation

Similarly, to clearly evaluate its vibration performance, the optimal VRG-MMD subjected to an increasing piston velocity profile (0-1.2[m/s]) has been investigated as shown in figure 14. The viscous damping coefficient is increasing as the piston velocity increases when no exciting currents are applied to the EMs. This is because the off-state damping exhibits nonlinear damping effects at high piton velocity ($\bar{V}_p$>1[m/s]). Figure 15 shows the force-displacement relationship both under triangle excitation at constant velocities (0.35, 0.75, 1.15[m/s]) and at different exciting current intensities through the EMs (0.5, 1.0, 1.5 [A]). It is also observed that compared to the T-MMD, the vibration performance of the optimal VRG-MMD is considerably improved in terms of the total damping force and dynamic range. The maximum damping force of the optimal VRG-MMD reaches 6000[N] at $\bar{V}_p$=0.75[m/s] and I_j=1.5[A]. These results of the performance evaluation directly indicates the importance and necessity of the optimization design for a multi-coil MR damper.

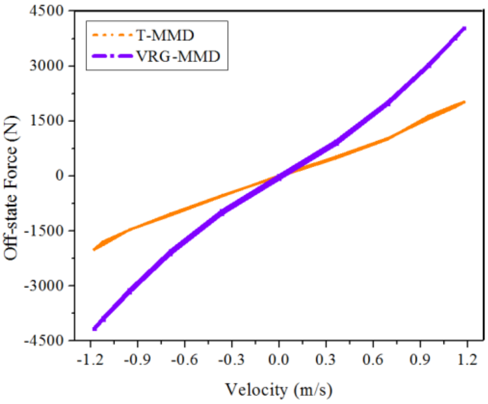

Fig 14 Off-state damping force vs. velocity

5. Conclusion

A novel design of the multi-coil MR damper with a variable resistance gap (VRG-MMD) has been designed evaluated. The performances of the initial VRG-MMD such as the total damping force, dynamic range and inductive time constant were investigated based on the multi-physics, namely, magnetic field and fluid dynamics. A simplified magnetic equivalent circuit was presented with four individual voltage sources. In such a way, the magnetic flux passing through each active gap can be understood as vector operations when four EMs are applied with individual exciting currents.

To find out the optimal design of the VRG-MMD constrained in a given volume, the FEM solution combined magnetic field with fluid dynamics was performed using Bound Optimization BY Quadratic Approximation (BOBYQA) technique. The geometric parameters (coil width W_c, pole radius R_{pi} and pole length L_{pi}) selected as the design variables (DVs), have been employed to solve an optimization problem. The multi-objective function was proposed using weighting method by taking the total damping force, dynamic range and inductive time constant into account. It has been demonstrated that the damping force and dynamic range are sensitive to the pole radius R_{pi} and the inductive time constant is sensitive to the pole length L_{pi}. The simulation results also show that the weighting factors of the multi-objective functions have a significant influence on the optimal geometry of the VRG-MMD.

Finally, the dynamic characteristics of the multi-coil dampers with equal weighting factors were studied by exerting external sinusoidal and triangle displacement excitations. The overall performance of the optimized VRG-MMD confirms a significant improvement in comparison with that of the T-MMD.

ACKNOWLEGEMENTS

This work has been supported by a Natural Science Foundation of China (NSFC) grant funded by the Chinese government (No.51175265 and No.51305207). This work was also supported by China Scholarship Council (CSC, No.201306840019).

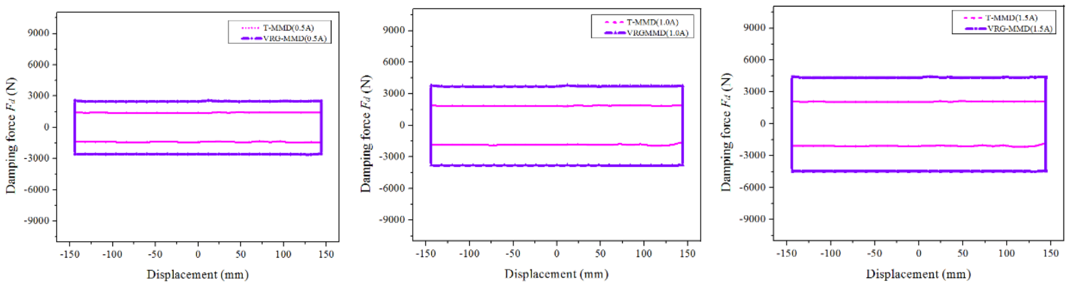

(a) (a_0=150[mm], $\bar{V}_p$=0.35[m/s])

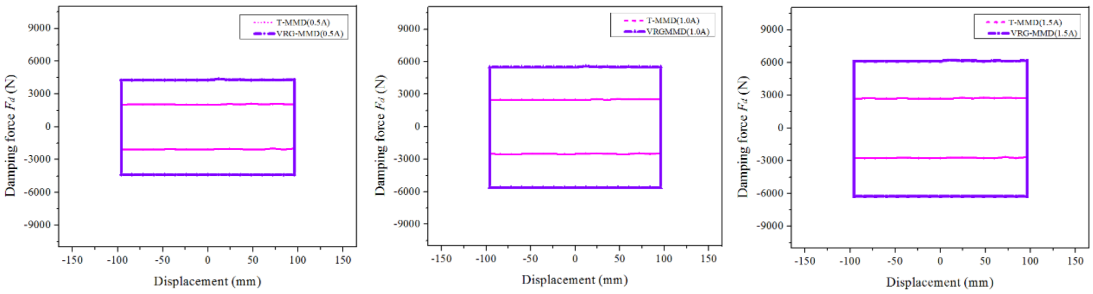

(b) (a_0=100[mm], $\bar{V}_p$=0.75[m/s])

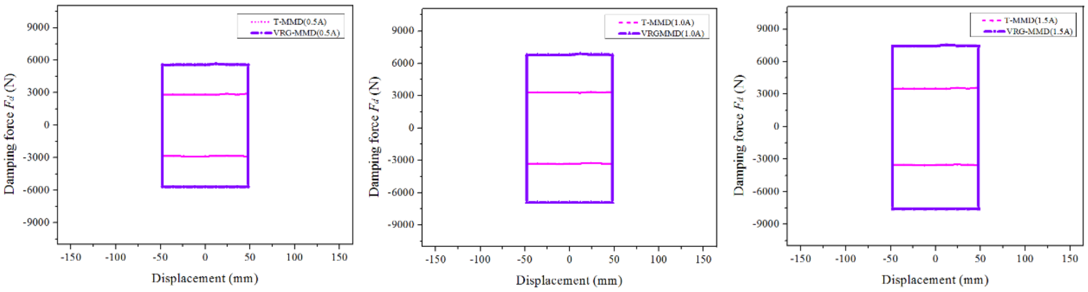

(c) (a_0=50[mm], $\bar{V}_p$=1.15[m/s])

Fig15 Damping force vs. displacement curve for currents 0.5A, 1A, 1.5A

Reference

[1]. Du Haiping, Kam Yim Sze, and James Lam. Semi-active H∞ control of vehicle suspension with magneto-rheological dampers. Journal of Sound and Vibration 283, no. 3 (2005): 981-996.

[2]. Hiemenz GJ, Hu W and Wereley NM (2008) Semi-active magnetorheological helicopter crew seat suspension for vibration isolation. Journal of Aircraft 45(3): 945–953

[3] Ok Seung-Yong, Dong-Seok Kim, Kwan-Soon Park, and Hyun-Moo Koh. Semi-active fuzzy control of cable-stayed bridges using magneto-rheological dampers. Engineering structures 29, no. 5 (2007): 776-788.

[4] Muhammad A, Yao XL and Deng ZC (2005) Review of magnetorheological (MR) fluids and its applications in vibration control. Journal of Marine Science and Application 5(3): 17–29.

[5] Batterbee DC, Sims ND, Stanway R, et al. (2007a) Magnetorheological landing gear 1: a design methodology. Smart Materials and Structures 16: 2429–2440.

[6] Batterbee DC, Sims ND, Stanway R, et al. (2007b) Magnetorheological landing gear 2: validation using experimental data. Smart Materials and Structures 16: 2441–2452.

[7] Powell Louise A., Wei Hu, and Norman M. Wereley. Magnetorheological fluid composites synthesized for helicopter landing gear applications. Journal of Intelligent Material Systems and Structures (2013): 1045389X13476153.

[8] Gudmundsson K. H., F. Jonsdottir, and F. Thorsteinsson. A geometrical optimization of a magneto-rheological rotary brake in a prosthetic knee. Smart Materials and Structures 19, no. 3 (2010): 035023.

[9] Xie Hua-Long, Ze-Zhong Liang, Fei Li, and Li-Xin Guo. The knee joint design and control of above-knee intelligent bionic leg based on magneto-rheological damper. International Journal of Automation and Computing 7, no. 3 (2010): 277-282.

[10] Mao Min, Wei Hu, Young-Tai Choi, and Norman M. Wereley. A magnetorheological damper with bifold valves for shock and vibration mitigation. Journal of Intelligent Material Systems and Structures 18, no. 12 (2007): 1227-1232.

[11] Bai Xian-Xu, Wei Hu, and Norman M. Wereley. Magnetorheological Damper Utilizing an Inner Bypass for Ground Vehicle Suspensions. Magnetics, IEEE Transactions on 49, no. 7 (2013): 3422-3425.

[12] Peng X and Li H 2007 Analysis of the magnetomechanical behavior of MRFs based on micromechanics incorporating a statistical approach Smart Mater. Struct. 16 2477–85.

[13] Singh Harinder J., Wei Hu, Norman M. Wereley, and William Glass. Experimental validation of a magnetorheological energy absorber design optimized for shock and impact loads. Smart Materials and Structures 23, no. 12 (2014): 125033.

[14] Nguyen QH, Han YM, Choi SB, et al. (2007) Geometry optimization of MR valves constrained in a specific volume using the finite element method. Smart Materials and Structures 16(6): 2242–2252.

[15] Nguyen QH, Choi SB and Wereley NM (2008) Optimal design of magnetorheological valves via a finite element method considering control energy and a time constant. Smart Materials and Structures 17: 025024 (12 pp.).

[16] Yang, L., Duan, F., and Eriksson, A., 2008, Analysis of the Optimal Design Strategy of a Magnetorheological Smart Structure, Smart Mater. Struct., 17(1), p. 015047.

[17] Parlak Zekeriya, Tahsin Engin, and İsmail Şahin. Optimal Magnetorheological Damper Configuration Using the Taguchi Experimental Design Method. Journal of Mechanical Design 135, no. 8 (2013): 081008.

[18] Rosenfeld NC and Wereley NM (2004) Volume-constrained optimization of magnetorheological and electrorheological valves and dampers. Smart Materials and Structures 13:1303–1313.

[19] Zhang, H. H., Liao, C. R., Chen, W. M., Huang, S. L., 2006, A Magnetic Design Method of MR Fluid Dampers and FEM Analysis on Magnetic Saturation, J. Intell. Mater. Syst. Struct., 17(8–9), pp. 813–818.

[20] Nguyen QH and Choi SB (2009a) Optimal design of MR shock absorber and application to vehicle

suspension. Smart Materials and Structures 18: 035012 (11 pp.).

[21] Nguyen QH and Choi SB (2009b) Optimal design of a vehicle magnetorheological damper considering the damping force and dynamic range. Smart Materials and Structures 18: 015013 (10 pp.).

[22] Karakoc K., Park, E. J., and Suleman, A., 2008, Design Considerations for an Automotive Magnetorheological Brake, Mechatronics, 18(8), pp. 434–447.

[23] Parlak Zekeriya, Tahsin Engin, and İsmail Çallı. Optimal design of MR damper via finite element analyses of fluid dynamic and magnetic field. Mechatronics22, no. 6 (2012): 890-903.

[24] Spencer J B F, Yang G, Carlson J D and Saint M K 1998 Smart dampers for seismic protection of structures: a full-scale study Proc. 2nd World Conf. on Structural Control (Kyoto, Japan) vol 1, pp 417–26

[25]. Zheng Jiajia, Zhaochun Li, JeongHoi Koo, and Jiong Wang. Magnetic Circuit Design and Multiphysics Analysis of a Novel MR Damper for Applications under High Velocity. Advances in Mechanical Engineering 2014 (2014).

[26] Güth Dirk, Markus Schamoni, and Jürgen Maas. Magnetic fluid control for viscous loss reduction of high-speed MRF brakes and clutches with well-defined fail-safe behavior. Smart Materials and Structures 22, no. 9 (2013): 094010.

[27] Hadadian Armin, Ramin Sedaghati, and Ebrahim Esmailzadeh. Design optimization of magnetorheological fluid valves using response surface method. Journal of Intelligent Material Systems and Structures (2013): 1045389X13504478.

[28] Nguyen Q. H., S. B. Choi, and K. S. Kim. Geometric optimal design of MR damper considering damping force, control energy and time constant. In Journal of Physics: Conference Series, vol. 149, no. 1, p. 012076. IOP Publishing, 2009.

[29] Nguyen QH, Choi SB, Lee YS, et al. (2009) An analytical method for the optimal design of the MR valve structure. Smart Materials and Structures 18: 095032 (12 pp.).

[30] White F M 1986 Fluid Mechanics 2nd edn (Blackick, OH: McGraw-Hill)

[31] Idelchik I E 2001 Handbook of Hydraulic Resistance 3rd edn (Redding, CT: CRC Begell House)

[32] Powell Michael JD. The BOBYQA algorithm for bound constrained optimization without derivatives. Cambridge NA Report NA2009/06, University of Cambridge, Cambridge (2009).

[33] Zhu Xiaocong, Xingjian Jing, and Li Cheng. Optimal design of control valves in magnetorheological fluid dampers using a nondimensional analytical method. Journal of intelligent material systems and structures 24, no. 1 (2013): 108-129.

[34] Yang, G., B. F. Spencer, J. D. Carlson, and M. K. Sain. Large-scale MR fluid dampers: modeling and dynamic performance considerations. Engineering structures 24, no. 3 (2002): 309-323.

[35] Spencer Jr, B. F., S. J. Dyke, M. K. Sain and JDf Carlson. Phenomenological model for magnetorheological dampers. Journal of engineering mechanics (1997).

Appendix

Nomenclature		T	Inductive time constant
L_t	Length of out cylinder	$P_{w,j}$	Power consumption by the ^{j}th EM
L_p	Length of piston head	F_τ	Damper yield force
L_f	Length of the filler	F_m	Damper minor loss force
i	Number of magnetic poles ($i = 1, \ldots, 5$)	F_η	Damper viscous force
j	Number of EMs ($j = 1, \ldots, 4$)	P_u	Upper chamber pressure
L_{pi}	Length of the ^{i}th magnetic pole	P_l	Lower chamber force
R_{pi}	Radius of the ^{i}th magnetic pole	$\tilde{A}_{pu}$	Area of upper effective piston
R_{in}	Radius of inner cylinder	$\tilde{A}_{pl}$	Area of lower effective piston
R_{oc}	Radius of out cylinder	ΔP	Pressure drop between upper and lower chamber
θ	Angle of the filler	ΔP_τ	Pressure drop due to yield stress
ϑ_{cj}	Magnetomotive force generated by the ^{j}th EM	ΔP_η	Pressure drop due to viscous effect
$\emptyset_{cj}$	Magnetic flux generated by the ^{j}th EM	F_d	Total damping force
$\emptyset_{cj}^{i}$	Magnetic flux of the ^{i}th effective region generated by the ^{j}th EM	ρ	Density of MR fluid
$\emptyset_{sum,i}$	Total magnetic flux of the ^{i}th effective region	τ_y^i	Yield stress of the ^{i}th effective region
$R_{m,ci}$	Resistor of ^{i}th MR fluid region	H_{mr}	Magnetic field intensity
$B_{mr,i}(s)$	Magnetic flux density at each nodal point on the ith defined path	K_{m_k}	Minor loss coefficient
$\bar{B}_{mr,i}$	Average magnetic flux density on the ith defined path	$\bar{V}_{m\_k}$	Corresponding average velocity associated with the minor loss coefficient
S_{pi}^{*}	Effective Area of the ^{i}th magnetic pole	$\bar{V}_i$	Average velocity of the ^{i}th active fluid region
ξ	Coefficient for the active region	$\bar{V}_j$	Average velocity of the ^{j}th inactive fluid region
I_j	Exciting current applied to the ^{j}th EM	$\bar{V}_p$	Average velocity of the input piton

R_w	Resistance of the coil wire	Re	Reynolds number
N_{cj}	Number of the ^{j}th coil turns	e	average pipe wall roughness
A_{cj}	Cross-sectional area of the EM	$\tilde{d}_{pc}$	Thickness of resistance gap
A_w	Cross-sectional area of the copper wire	k	Coefficient for fitting yield stress
D_{cw}	The diameter of the copper wire	λ	Dynamic range
$\tilde{r}$	The resistivity of the copper wire	α, β, γ	Weighting factors of the objective function
ϵ	Coefficient for rolling copper wire	F_{dr}	Reference total damping force
f	Objective function	λ_r	Reference dynamic range
f_D	Darcy friction factor in MR damper	T_r	Reference inductive time constant
m	Maximum number of EMs	n	Maximum number of magnetic poles $(n = m + 1)$